Catena 107 (2013) 57–70

Contents lists available at SciVerse ScienceDirect

Catena

journal homepage: www.elsevier.com/locate/catena

Mapping the distribution of weathered Pleistocene wadi deposits in Southern Jordan using ASTER, SPOT-5 data and laboratory spectroscopic analysis

Rene Löhrer [a,*], Manuel Bertrams [a], Eileen Eckmeier [b], Jens Protze [a], Frank Lehmkuhl [a]

[a] Department of Geography, RWTH Aachen University, Wüllnerstr. 5b, D-52056 Aachen, Germany
[b] Institute of Crop Science and Resource Conservation (INRES), Soil Science and Soil Ecology, University of Bonn, Nußallee 13, D-53115 Bonn, Germany

ARTICLE INFO

Article history:
Received 12 October 2012
Received in revised form 31 January 2013
Accepted 4 February 2013

Keywords:
Remote sensing
GIS
Spectroscopy
Geoarchaeology
Iron oxides
Jordan

ABSTRACT

In the arid regions of the Levant, ancient wadi fills act as a terrestrial sedimentary archive with a high potential for preserving archaeological findings. This current study combines remote sensing with laboratory VIS-spectroscopy to investigate the spatial distribution of alluvial wadi fills in a small catchment in Southern Jordan. Due to its homogeneous sandstone geology, the composition of the alluvial sediments is highly influenced by the local bedrock whilst fluvial relocation and surface weathering processes initiated a secondary alteration of dominant iron oxides (Fe^{3+}). The differences in mineralogical composition of the sediments enable the detection and mapping of wadi deposits by remote sensing using different spectral combinations of ASTER and SPOT-5 satellite images. Additionally, laboratory measurements of reflectance spectra were applied on selected surface samples and soil sections from the study area in order to verify the information derived from remote sensing and to quantify the degree of surface weathering and pedogenic processes. The results show that an initial transformation from hematite to goethite is the dominant process related to the recent arid conditions in the study area. Furthermore, it is possible to predict potential new archaeological finding areas using remote sensing techniques.

1. Introduction

Advances in the prospection of archaeological sites help propel the investigation of environmental interactions and migration pathways of early modern humans from their origin in Africa towards Europe. In Southern Jordan, archaeological findings embedded in reddish Pleistocene wadi deposits manifest the occurrence of anatomically modern humans (*Homo sapiens sapiens*). As the study area is located at the border of a potential convergence area between *Homo sapiens sapiens* and *Homo neanderthalensis* (e.g. Bar-Yosef, 2002; Bar-Yosef et al., 1986; Hublin, 2009; Mellars, 2004, 2006; Richter et al., 2012; Stringer, 2002), the spatial distribution of these Palaeolithic sites and related sediments is particularly important for investigating the settlement history of the Levantine region. Typically, landscape dynamics and environmental settings of human settlements are analysed according to two different scales. In this study, the larger scale covered by remote sensing is used to obtain information about the spatial distribution of artefact-bearing wadi sediments by assessing variations in iron oxide mineralogy (Bierwirth, 1990; Hewson et al., 2001; Hubbard et al., 2007; Kalinowski and Oliver, 2004; Mars and Rowan, 2011; Rowan and Mars, 2003; Shafique et al., 2011a,b). This larger scale mapping generates information about areas with different concentrations of iron oxides, thereby enabling researchers to delineate between Pleistocene wadi fills and derivative bedrock sandstone formations (cf. Fig. 3). At locations with high concentrations of ferric iron (Fe^{3+}), sediment samples for the smaller scale laboratory analysis were taken to verify rubification processes and to inspect the environmental development of the sediments (Ben-Dor et al., 2002, 2006; Grunert et al., 2007; Scheinost and Schwertmann, 1999; Scheinost et al., 1998; Torrent et al., 1983). Based on the degree of post-depositional alteration of iron oxides in wadi deposits, both approaches can be combined and exploited as a prospection tool for potential archaeological find spots in sandstone dominated environments.

Due to a lack of moisture and organic matter in this recently arid environment, the colour of sediments and soils is mainly attributed to iron oxides (Folk, 1976; Walker, 1974). The reddish colour (Fig. 1) can either be primarily derived from local bedrock or result from an intense weathering of iron-bearing material, thereby inducing a secondary alteration. In this process of rubification, iron is released from less stable minerals in the form of ferrihydrite [$(Fe^{3+})_2O_3 \cdot 0.5H_2O$] and subsequently transformed into more stable forms such as hematite [Fe_2O_3] or goethite [$FeO(OH)$] under oxidizing conditions (Gardner, 1981; Schwertmann, 1959; Schwertmann and Cornell, 2000).

In soils from tropical and subtropical regions, hematite and goethite are the predominant stable Fe^{3+} minerals, both descending

* Corresponding author. Tel.: +49 241 8096052; fax: +49 241 8092460.
E-mail address: loehrer@geo.rwth-aachen.de (R. Löhrer).

0341-8162/$ – see front matter © 2013 Elsevier B.V. All rights reserved.
http://dx.doi.org/10.1016/j.catena.2013.02.003

Fig. 1. Reddish wadi deposits and adjacent bedrocks in the Wadi Sabra, Southern Jordan.

from the unstable ferrihydrite in two parallel synthetic reactions. Whereas goethite is commonly formed under moderate climate conditions, higher temperatures and dry climate lead to the formation of hematite. The conversion of hematite to the more yellowish goethite generally results from a selective dissolution of hematite by reduction or complexation under the influence of microorganisms or organic substances but is not related to chemical affiliation of water (Cornell and Schwertmann, 2003; Nagano et al., 1994; Schwertmann, 1966, 1969; Schwertmann and Cornell, 2000). Consequently, the formation of goethite in surface soils of arid environments is not uncommon but more time-consuming due to the low availability of moisture.

To understand the spatial distribution and the geological sources of the red sediments, remote sensing and Geographical Information Systems (GIS) techniques supported by laboratory colour spectrophotometry are applied. The mapping of the spatial distribution of sediments coloured by iron oxides could enable the prediction of possible archaeological find spots.

The objective of the current study is to address the following questions:

- Are sediments with high Fe^{3+} content in this study area detectable by remote sensing analysis of ASTER and SPOT-5 satellite images?
- Do direct laboratory measurements of VIS-spectra from sediments in an archaeological context support the information derived by remote sensing?
- Can new potential find spots be estimated for archaeological research?

2. Regional setting

The study area is situated at the eastern rim of the Jordan Rift Valley in South Central Jordan (Fig. 2A). The tectonically active transform fault is one of the main mechanisms for geomorphological processes. East of the Wadi Araba, a zone of deeply incised wadi systems ascend to the highland plateau of Al-Jafr that is associated with the deserts of the Arabian Peninsula. The Wadi Sabra begins a few kilometres southwest of the ancient Nabataean capital of Petra and drains in a total length of about 22 km into a vast alluvial fan of the Wadi Araba. In its 90 km^2 wide catchment area, elevations reach from 216 m to 1713 m a.s.l. In the upper reaches, the wadi is partially filled by large remnants of Pleistocene sandy wadi deposits (Fig. 2B) that consist of erosional products of the surrounding bedrocks (Bertrams et al., 2012).

Fig. 2C shows an E–W geological cross-section of the study area. The region is mainly characterised by the reddish Cambrian–Ordovician Umm Ishrin sandstone formation. This complex of quartzic, red to brown coloured and planar through cross-bedded sandstones is the main source rock for the fluvial wadi fills. Rhythmic deposition of manganese and iron oxides resulted in the characteristic colourful banding of this braid-plain deposited quartz–arenite facies (Barjous, 2003; Makhlouf and Abed, 1991). Towards the eastern plateau, the sandstones are covered by Cretaceous limestone beds providing the minor content of carbonate to the wadi fills that locally induced solidification and, thus, promoted resistance to erosion. The transition zone between semi-arid Mediterranean and arid desert climate is characterised by an average annual temperature of 17–20 °C and an annual precipitation ranging from <100 mm in the lower part to 100–200 mm in the upper part of the catchment. Consequently, the vegetation cover is controlled by the climatic conditions in different altitudes. In the highest parts of the study area, sparse juniper forests alternate with oak forests. Down towards the Jordan Valley, Mediterranean scrubs are replaced by steppe, desert and saxicolous plants, respectively (Royal Jordanian Geographic Centre, 2007).

As precipitation is restricted to intense rainfall often occurring during winter, the study area is a highly dynamic environment presently dominated by erosional processes. Consequently, the Pleistocene wadi deposits have the highest potential for a preservation of in-situ archaeological sites that confirm human occupation during Upper Palaeolithic times.

First archaeological investigations of the Palaeolithic and Neolithic in the Wadi Sabra area were conducted by Gebel (1983, 1988) and Schyle and Uerpmann (1988). Renewed fieldwork took place during two field campaigns in 2009 and 2010, resulting in the discovery of additional sites (Bertrams et al., 2012). The majority of sites are attributed to the Upper Palaeolithic (~50–15 ka). However, the complete Palaeolithic sequence of the Southern Levant is represented either as completely preserved in-situ find layers or at least as single surface finds which have been affected by erosional processes that began during the Holocene and prevailed until modern times.

From these studies, 13 site locations with finds embedded within the wadi sediments were selected for remote sensing applications (Table 1). Most of these sites are situated within the northern part of the Wadi Sabra (Fig. 2A). The measured reflectance values represent the current stage of iron oxide weathering at the recent surface and do not give direct information on the palaeoenvironmental conditions during the time of human occupation. The latter have been investigated in another study. The present research only focuses on surface characteristics and recent weathering dynamics to delineate artefact-bearing sediments from bedrock materials.

3. Methods

3.1. Remote sensing

The analysis of digital data was based on the combination of remote sensing and GIS (Geographical Information Systems) using ESRI Arc GIS 10 and PCI Geomatica 10.3.1 as primary tools. The remote sensing data was interpreted using ASTER (Advanced Spaceborne Thermal Emission and Reflection Radiometer) and SPOT-5 (Système Pour l'Observation de la Terre) satellite images (Fig. 2A).

The ASTER instrument is based on the NASA Terra satellite, which is part of the Earth Observing System. It provides high-resolution images of various bands from visible to infrared wavelength in different resolutions (Table 2). The swath width of each scene averages 60 km × 60 km.

The analysed scene was received on September 16, 2002 with 0% cloud cover. In a first step, the hierarchical data format was transferred into a common ERDAS Imagine format and registered to UTM 36R. The ATCOR module of PCI Geomatica was used for the atmospheric

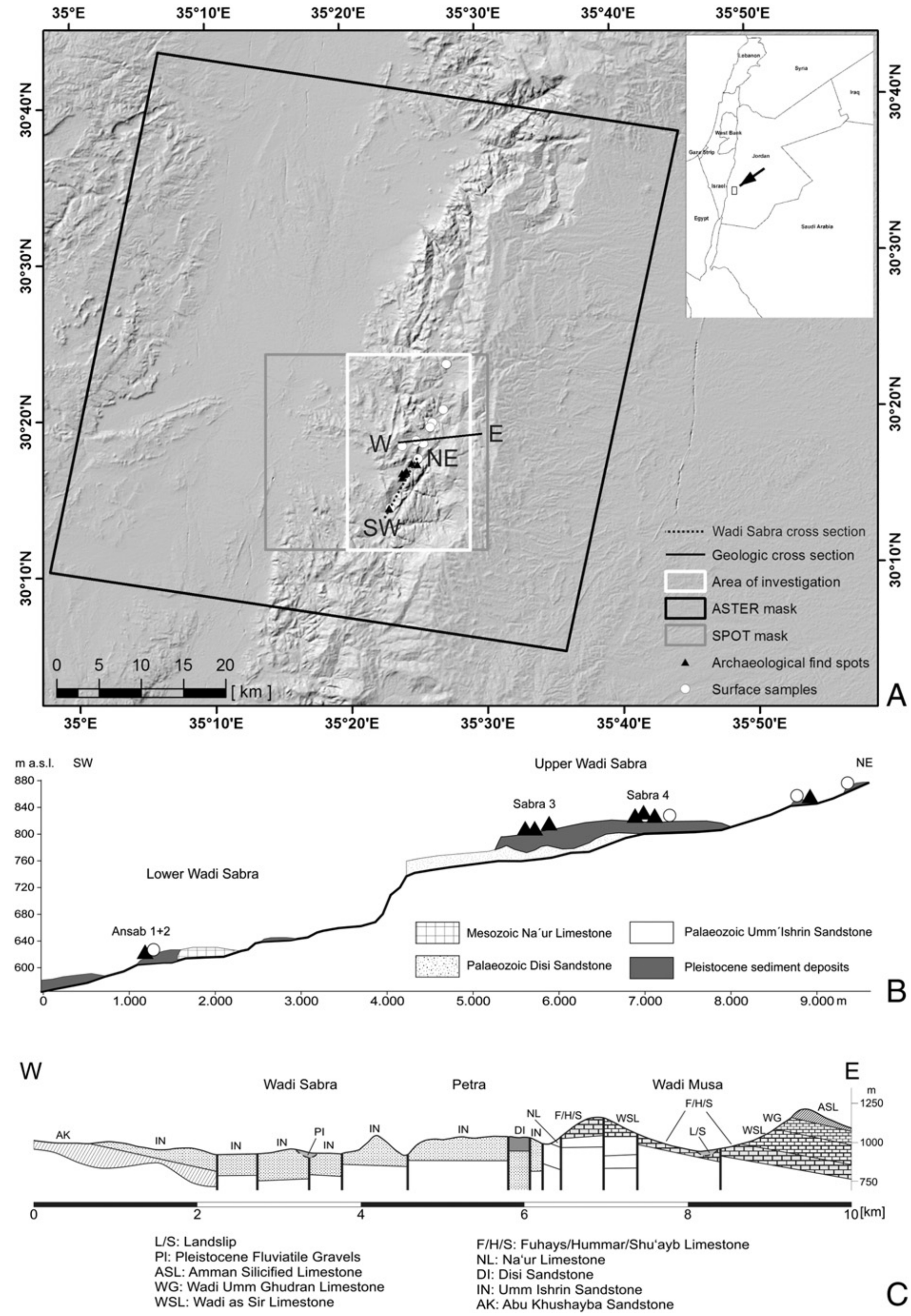

Fig. 2. (A) Area of investigation in Southern Jordan. (B) Longitudinal cross-section of the Wadi Sabra valley bottom showing the spatial distribution of major wadi deposits. (C) Geologic cross-section through the study area (modified according to Barjous, 2003).

correction of the ASTER image. Due to this process, the digital numbers of the single ASTER channels were corrected to radiance at sensor as follows:

$$Radiance = (digital\ number - 1) * \text{“}unit\ conversion\ coefficient\text{”}. \qquad (1)$$

The unit conversion coefficient was obtained from the metadata of the ASTER scene and a calibration file for the atmospheric correction was generated (Table 3).

In addition, the elevation information for that correction was gathered from an ASTER GDEM elevation model (ASTER GDEM, 2010).

The interpretation focused on identifying certain minerals from reflectance spectra to support the sedimentological analysis, thereby providing information on the intensity and progress of surface weathering processes in the investigated area. Basic research on the identification of minerals from ASTER images had been conducted by several authors (e.g. Abrams, 2000; Abrams and Hook, 1995; Bierwirth, 1990; Crowley, 1993; Hewson et al., 2001; Hubbard et al., 2007; Kalinowski and Oliver, 2004; Mars and Rowan, 2006, 2011; Ninomiya and Fu, 2001; Rowan and Mars, 2003; Rowan et al., 2003; Yamaguchi et al., 1998). They used different combinations and ratios of ASTER bands to identify specific minerals based on their spectral reflectance. These studies commonly focused on detecting minerals from satellite images to acquire information about potential mining sites. In this current study, however this approach was employed to generate information about the spatial distribution of sediments in which archaeological finds are potentially embedded.

The occurrence and alteration of iron from Fe^{2+} to Fe^{3+} was used to evaluate weathering intensities and to delineate the Pleistocene

Table 1
Archaeological records from the Wadi Sabra, Southern Jordan.

Location	Longitude (E)	Latitude (N)	Type
Sabra 2010/4	35° 24′ 20.87″	30° 16′ 24.23″	Levallois-Mousterien
Sabra 2010/15	35° 24′ 12.95″	30° 16′ 17.03″	Levallois-Mousterien
Sabra 2010/2	35° 24′ 18.00″	30° 16′ 22.43″	Levantine Aurignacian
Sabra 2010/6	35° 24′ 10.07″	30° 16′ 13.07″	Levantine Aurignacian
Sabra 2010/10	35° 24′ 43.56″	30° 16′ 54.48″	Natufian
Sabra 2010/25	35° 25′ 09.11″	30° 16′ 49.44″	Natufian
Sabra 1	35° 24′ 01.08″	30° 16′ 17.03″	Geometric Kebaran, Natufian, Neolithic
Sabra 4 Palmview 1	35° 24′ 17.63″	30° 16′ 18.47″	Levantine Aurignacian
Sabra 4 Palmview 3	35° 24′ 17.28″	30° 16′ 19.55″	Levantine Aurignacian
Sabra 3 Centre	35° 24′ 02.52″	30° 16′ 01.55″	Qalkhan
Sabra 3 South	35° 24′ 02.52″	30° 16′ 00.47″	Kebaran
Ansab 2	35° 23′ 00.59″	30° 14′ 03.84″	Initial Upper Palaeolithic
Ansab 1	35° 22′ 59.52″	30° 14′ 03.12″	Ahmarian

sediments. The abundance of Fe^{3+} was determined by a band ratio of 2/1 and class ranges were automatically defined with a 1/3 standard deviation. Additionally, low values for the ratio $5/3+1/2$ for the Fe^{2+} content were used to control this classification (Hewson et al., 2006; Kalinowski and Oliver, 2004; Rowan and Mars, 2003). To isolate those areas with high abundance of Fe^{3+}, a differentiation threshold to Fe^{2+} regions was calculated with a 2σ interval. Thus, 5.58% of the pixels with the value one in the new grid represented the areas characterised by high Fe^{3+} values (Fig. 4).

The red Pleistocene sediments were clearly visible in the true colour SPOT-5 satellite image of the study area. Subsequently, this image was used to support and validate the classification of the ASTER image. The "Système Pour l'Observation de la Terre" in the fifth generation (SPOT-5) provides high spatial resolution images by using two High Resolution Geometric (HRG) instruments. The HRG includes one panchromatic band, three multispectral bands and one short-wave infrared band in different resolutions (Table 4). The swath width of each scene averages from 60 km×60 km to 80 km×80 km (Lillesand et al., 2004).

Fig. 2A shows the spatial mask of the SPOT-5 panchromatic-colour image which is a composite image of the years 2007 (3%), 2009 (82%) and 2010 (15%). To obtain an image with a spatial resolution of 2.5 m, it was necessary to combine the panchromatic images with the 5 m colour images (SPOT IMAGE, 2011).

Based on the SPOT-5 image, a supervised classification was applied with the Gaussian maximum likelihood classifier which is one of the widely used algorithms for supervised classifications in different scales (e.g. Defries and Townshend, 1994; Mickus and Johnson, 2001). The algorithm assumes that every object class has a normal distribution around the predefined centre selected by manually digitised training sites. An unknown pixel is assigned to an object class by evaluating the covariance and the variance of the pixel (Lillesand et al., 2004).

At first, areas of similar surface reflection close to the locations of the archaeological find spots were isolated, representing the training sites (Fig. 2A). These training sites were only used for the SPOT-5 classification because the produced ASTER grid was a seamless mapping of the iron oxide distribution. A sufficient number of training sites were evaluated by the signature separation statistic of Bhattacharyya (1943) creating seven probability classes and a null class. Seven classes were chosen because the spectral signatures of the training sites in the Wadi Sabra allowed a differentiation of those mentioned classes. Normally, it is useful to make an accuracy assessment based on the number of error pixels, as the classification has to be performed for the whole image. However, since the training sites used for the SPOT-5 classification were concentrated exclusively within the Wadi Sabra, the checking for a correct pixel assignment including the area outside of the wadi was not reasonable.

Table 3
Calibration file for the ATCOR process (9 = ASTER channel, c0 = offset, c1 = corrected gain).

9	c0	c1 [mW/cm^2 sr micron]
1	−0.1	0.06760
2	−0.1	0.07080
3	−0.1	0.08620
4	−0.1	0.02174
5	−0.1	0.00696
6	−0.1	0.00625
7	−0.1	0.00597
8	−0.1	0.00417
9	−0.1	0.00318

A value of one was assigned to the classes 1, 2 & 6 of the SPOT-5 classification. Finally, this grid was combined with the obtained ASTER grid by an Arc Map conditional algebra statement:

$$Con((\text{"}ASTER\_reclass\text{"} == 1) \& (\text{"}SPOT\_reclass\text{"} == 1), 1). \quad (2)$$

This equation only identifies areas where pixels are found in the classified SPOT-5 image and the ASTER grid. These pixels represent the most promising areas for the location of in-situ sites and have to be evaluated by future systematic archaeological surveys.

3.2. Field and laboratory methods

During a field campaign in 2010, 15 sediment samples from the surface were collected from locations with a high absorption in the ASTER Fe^{3+} band combination (Table 5). These samples were intended to verify the geochemical properties of the sediments and to evaluate the spectral reflectance of the chosen ASTER band combination. Moreover, they were used for further calibration to support detailed remote sensing. Topsoil sections with a maximum depth of 100 cm were sampled in the context of archaeological excavations at the sites of Ansab 1 + 2 and Sabra 4 (Fig. 2B, Table 1) in order to capture subsurface weathering processes in different parts of the study area. These sections consist of fluvial deposited sands without any horizontation affected by percolating rainwater and root penetration during the winter season but which remain unaffected by surface relocation or aeolian deposition. For a determination of background values, additional sample material was collected from local bedrock formations (samples Qx3 and Qx4) and recent channel deposits (Qa1).

Iron oxides were identified by colorimetric measurements of the collected samples. In order to qualitatively describe soil colour, the

Table 2
Spectral channels of the ASTER instrument.

	Visible and near infrared (VNIR)	Shortwave infrared (SWIR)	Thermal infrared (TIR)
Spectral range	Band 1: 0.52–0.60 µm Band 2: 0.63–0.69 µm Band 3: 0.76–0.86 µm	Band 4: 1.600–1.700 µm Band 5: 2.145–2.185 µm Band 6: 2.185–2.225 µm Band 7: 2.235–2.285 µm Band 8: 2.295–2.365 µm Band 9: 2.360–2.430 µm	Band 10: 8.125–8.475 µm Band 11: 8.475–8.825 µm Band 12: 8.925–9.275 µm Band 13: 10.25–10.95 µm Band 14: 10.95–11.65 µm
Resolution	15 m	30 m	90 m

Table 4
Spectral channels of the SPOT-5 instrument.

	Panchromatic	Visible and near infrared (VNIR)	Shortwave infrared (SWIR)
Spectral range	Pan.: 0.48–0.71 μm	Band 1: 0.50–0.59 μm	Band 4: 1.58–1.75 μm
		Band 2: 0.61–0.68 μm	
		Band 3: 0.78–0.89 μm	
Ground resolution	5 m or 2.5 m	10 m	20 m

Munsell notification (Munsell Color Company Inc., 1975) and the CIE LAB system (Commission Internationale de l'Eclairage, 1978) are the most frequently methods used in geoscientific research (Mathieu et al., 1998; Torrent and Barrón, 1993). These systems help to reliably identify different iron oxides (Scheinost and Schwertmann, 1999), since the spectral properties of the samples are clearly influenced by the major iron oxide(s).

Soil colour was measured for dried and homogenised soil samples (particle sizes <2 mm) in triplicates using a spectrophotometer (Konica Minolta CM-5) by detecting the diffused reflected light under standardised observation conditions (2° standard observer, illuminant C). The colour spectra were obtained in the range of visible light (VIS), from 360 nm to 740 nm, in 10 nm increments. The spectral information was converted into the Munsell colour system and the CIELAB Colour Space (CIE 1976 $L^*a^*b^*$) using the Software SpectraMagic NX (Konica Minolta). The $L^*a^*b^*$ values indicate the extinction of light, or luminance, on a scale from L^* 0 (absolute black) to L^* 100 (absolute white), and express colour as chromacity coordinates on red-green (a^*) and blue-yellow (b^*) scales. A bivariate plot of the CIE a^*- and b^*-values (according to Nagano et al., 1994) was used to illustrate the relation of sample colour to local source materials on iron oxide weathering paths from the instable ferrihydrite to the stable forms of hematite (along the a^*-axis) and goethite (along the b^*-axis).

The prediction of hematite content from the colour should always be based on data obtained from materials, which are similar to the ones being studied (Torrent et al., 1983). Consequently, the Redness Rating $[RR(MUN) = (10 - H) * C/V]$ was used with an inverse function of the linear regression obtained from European soil material (according to Torrent et al., 1983). Additionally, the first derivative of the reflectance spectra was calculated, and the continuum-removed absorption analysis (Ben-Dor et al., 2006; Clark et al., 1987) was applied to the spectral data to enhance the absorption features and to intensify the relation of hematite and goethite in the samples compared to spectral data of synthetic iron oxides derived from the ASTER Spectral Library (Baldridge et al., 2009; Grove et al., 1992).

Table 5
Surface samples with indications of high Fe^{3+} content in the ASTER satellite picture.

Sample	UTM 36R easting	UTM 36R northing	DD longitude	DD latitude
Goe01	735781	3358870	35.4527	30.3387
Goe02	733418	3354826	35.4272	30.3027
Goe04	730911	3354511	35.4011	30.3004
Goe05	732567	3355192	35.4184	30.3062
Goe09	734467	3357328	35.4387	30.3251
Goe10	734200	3356776	35.4358	30.3202
Goe11	732235	3352262	35.4143	30.2798
Goe12	732339	3352426	35.4155	30.2813
Goe13	732687	3352912	35.4192	30.2856
Goe14	732743	3352996	35.4198	30.2864
Goe14b	732743	3352996	35.4198	30.2864
Goe15	732805	3353086	35.4204	30.2872
Goe18	729507	3347192	35.3849	30.2346
Goe19	736116	3364229	35.4573	30.3870
Goe19b	736182	3364182	35.4580	30.3865

4. Results

4.1. Remote sensing

Fig. 3 depicts the distribution of iron oxides in the investigation area. The chosen band combination of the ASTER image B2/B1 indicates low (blue colours) and high values (red colours) of Fe^{3+} content. The values of the grid are stretched. This results in an undetermined differentiation of the iron oxides. To eliminate unwanted reflections from settlement structures in the image, a threshold of the 95% quantile of the standard deviation was set. As a result, those areas with a high Fe^{3+} content are indicated in an area comprising 18.7 km^2 (Fig. 4).

Generally, high Fe^{3+} concentrations are located in the valleys, and lower concentrations thereof are found on the top of the mountains. The highest concentration of Fe^{3+} can be found in the centre of the image in deeply incised wadis. Another area with increased Fe^{3+} concentration is located in the south-western corner of the image indicating a dune field. To separate and consolidate these areas, the supervised classification of reddish signatures in a SPOT-5 image was applied.

Seven different types of characteristic spectral reflections in the valley of the Wadi Sabra were analysed using the selected training sites. The statistics (Table 6) show a very good average separability of 1.99, with a maximum at 2.0 and a minimum at 1.86. A separability value of 2.0 indicates a proper pixel separation with no more pixel overlap.

The signature statistics of the training sites (Table 7) give an overview of the mean and the standard deviation of different bands of the SPOT-5 satellite image. The average standard deviation is 3.63 with a maximum of 6.83 in band 3 of class 6 and a minimum of 1.88 in band 2 of class 5. This shows the setup quality of the training sites. The area of the training sets for class 1 is significantly larger than that of other sets. The characteristic spectral reflections of class 1 training sites are widespread in the valley and provide much more possible surfaces for the resulting classification. The other training sets cover almost nearly the same area.

The results of the classification related to the number of classified pixels and the area are shown in Table 8. The complete investigation area comprises 336 km^2. Class 1 has the smallest classified area with only 2.41 km^2, but it covers most of the training sites. This ratio is an indicator for the quality of the choice of the training sets. The confusion matrix (Table 9) presents the percentage of pixels classified by the setting of training areas that will be removed in another class by applying the maximum likelihood algorithm. The average accuracy of 95.07% with a confidence interval of ± 0.92 for 95% and a KAPPA coefficient of 0.92 with a standard deviation of 0.004 is further statistical proof of the quality of the visual choice of the training sites (Table 9).

This classification result with the highest probability of red signals was reclassified to a grid with one single value (Fig. 5). The area that contains this value amounts to 6.99 km^2.

As a final step of the image interpretation, both of the images were combined by a conditional statement (cf. Eq. (2)). In effect, the result is based both on a supervised classification with a SPOT-5 image and an unsupervised classified ASTER image. Fig. 6 shows those areas with an estimated high content of Fe^{3+} as a weathering product of the surrounding geology. This area is reduced to 6.32 km^2 in contrast to the area of the SPOT-5 classification (6.99 km^2) and the ASTER classification of 18.7 km^2.

4.2. VIS-spectroscopy

The 15 investigated surface samples plot in the YR-range of the Munsell colour system (3.7–8.7 YR, Fig. 7) which is defined as the area with mixed influence of both hematite and goethite (Schwertmann and Cornell, 2000). Furthermore, the bivariate plot of the CIE a^* and b^*

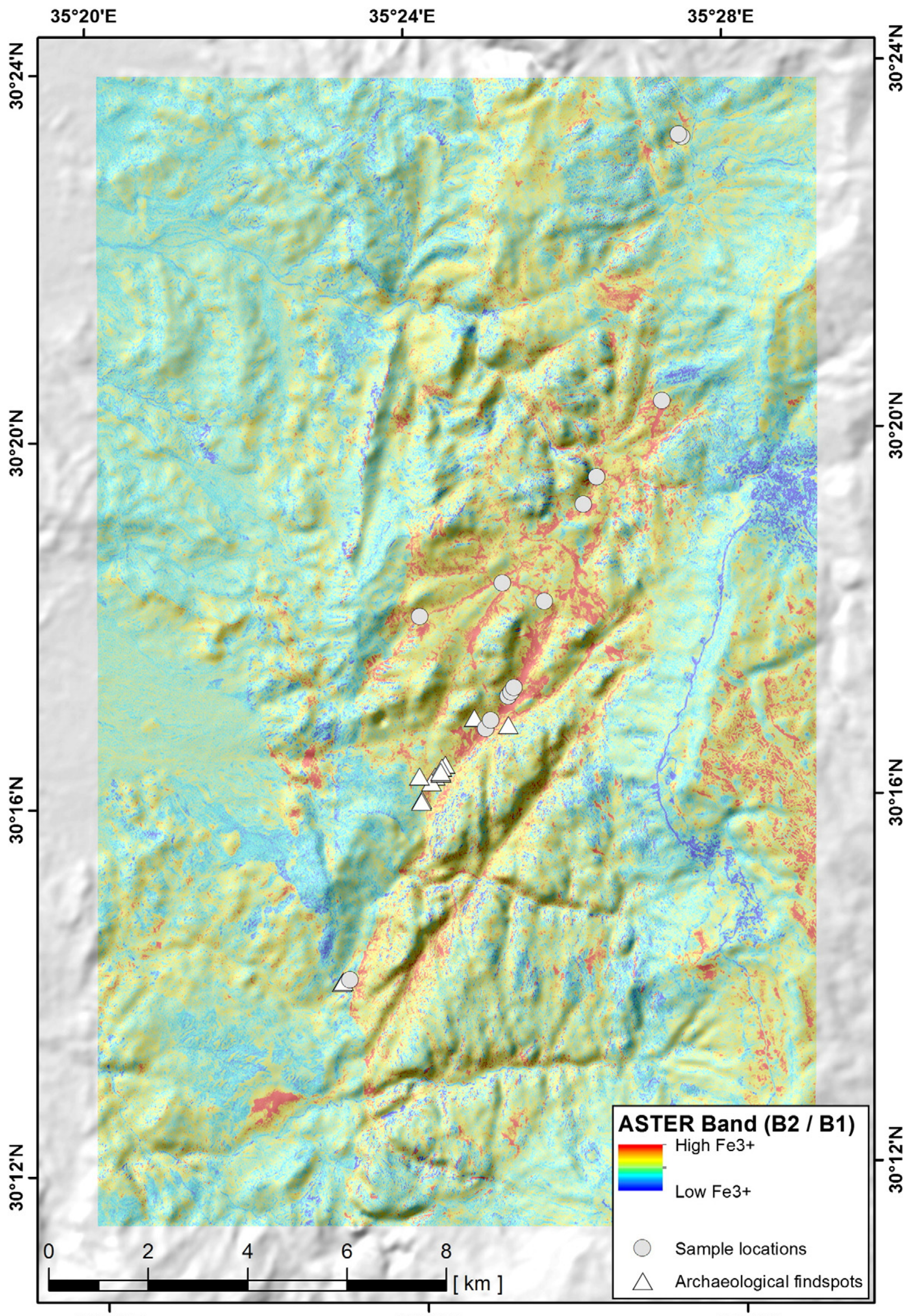

Fig. 3. Stretched ASTER image with the band combination (B2/B1) showing high concentrations of ferric iron (Fe^{3+}) in red and lower concentrations in blue. At the areas with the highest values, surface samples (dots) were collected for laboratory analysis to verify the remote sensing analysis of the ASTER image.

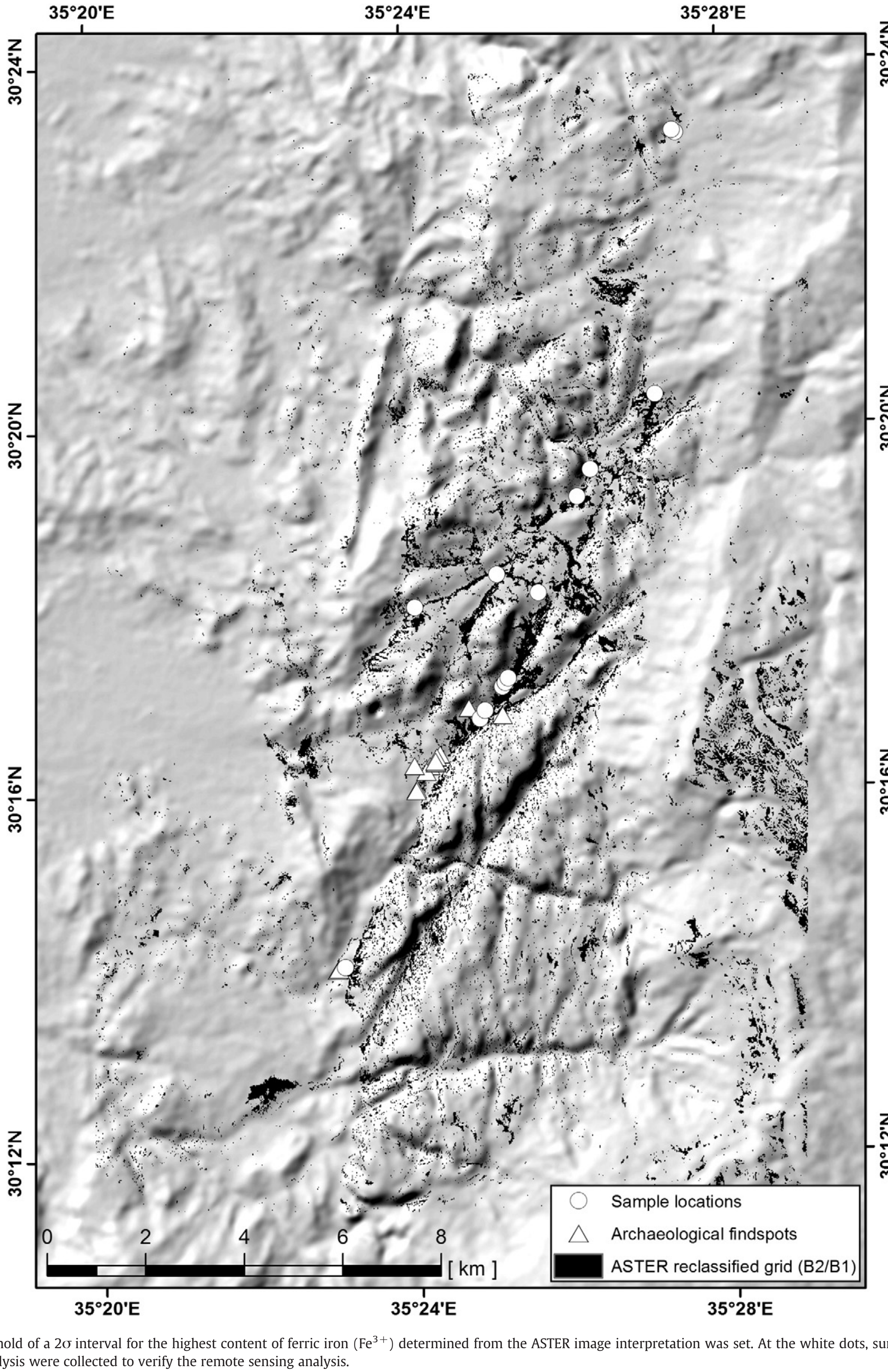

Fig. 4. A threshold of a 2σ interval for the highest content of ferric iron (Fe^{3+}) determined from the ASTER image interpretation was set. At the white dots, surface samples for laboratory analysis were collected to verify the remote sensing analysis.

Table 6
Signature separability of the training sites.

Separability measure	Bhattacharyya distance						
Average separability	1.98797						
Minimum separability	1.86390						
Maximum separability	2.00000						
	Class 1	Class 2	Class 3	Class 4	Class 5	Class 6	Class 7
Class 1							
Class 2	1.999995						
Class 3	1.995614	1.979590					
Class 4	2.000000	2.000000	2.000000				
Class 5	1.999524	2.000000	1.976130	2.000000			
Class 6	1.999998	2.000000	2.000000	1.997712	2.000000		
Class 7	2.000000	2.000000	2.000000	1.934894	2.000000	1.863969	

values (cf. chapter 3.2) provides a good discrimination of the progress of iron oxide weathering. However, most samples show a close relation to the bedrock samples of the local Umm Ishrin sandstone formation. Although a general tendency towards decreasing a*-values, i.e. decreasing redness, provides first evidence for initial weathering and a potential release of Fe^{3+}, the b*-values (yellow colour component) show only minor variations. Thus, the position of the samples data in this plot does not indicate the dominance of a specific iron oxide (Fig. 7).

Whilst quartz has featureless characteristics in the visible spectrum, hematite and goethite in their pure forms hold significant spectral signatures, which make them easily distinguishable (Ben-Dor et al., 2006; Grove et al., 1992). In the VIS range, free iron oxides are spectrally active due to the single electron transitions ($^6A_1 \rightarrow {}^4E; {}^4A_1$ around 380–440 nm and $^6A_1 \rightarrow {}^4T_2$ around 650–700 nm) and the electron-pair transition ($^6A_1 + {}^6A_1 \rightarrow {}^4T_1 + {}^4T_1$ around 480–540 nm) which are responsible for the Fe absorption of radiation that induces the red colour of soils (Ben-Dor et al., 2006; Scheinost et al., 1998; Sherman and Waite, 1985). Mainly the latter transition determines the position of the absorption edge that is already recognisable in the visible reflectance spectra of the observed surface samples and synthetic iron oxides (Fig. 8A + B). This effect is intensified by calculating the first derivative of the spectral reflectance data for each sample and mineral. From this plot, it is clearly observable that the absorption bands of synthetic hematite and goethite are dislocated and the spectral characteristics of the investigated surface samples and topsoil sections are influenced by a mixture of both iron oxides (Fig. 8C + D).

The close relation between surface and bedrock material is also shown by the continuum removal (CR) analysis. This method enhances the absorption features and allows a clearer separation of characteristic mineral signatures in the spectrum (Fig. 8 E + F). The two samples taken from the local Umm Ishrin sandstone formation (Qx3 and Qx4) have a spectral signature clearly affected by hematite with a dominant absorption feature (minimal turning point in the CR-curve) around 530 nm. Most surface samples (e.g. GOE1, 10, 12) show minor variations from the bedrock spectra, thus indicating less pronounced surface weathering and a dominance of hematite as colouring agent. However, some of the surface samples (e.g. GOE5, 18, 19a, 19b) depict a clear secondary alteration of the primary signal, indicated by a shift of the dominant absorption feature from 535 nm (clearly hematite dominated) towards 485 nm (goethite dominance) and by a second minor absorption feature appearing in the range of 420–430 nm which is also related to an increasing influence of goethite.

Overall, the samples taken from three topsoil sections in the upper and lower part of the catchment show no significant differences in reflectance spectra related to the bedrock and surface sediments (Fig. 8A + C). Moreover, there are no detected variations in the profile with respect to altitude, morphological position or depth. This infers that the process of iron oxide weathering is mostly inhibited in the subsurface area.

The calculation of hematite content from the redness rating values (Fig. 9) finally shows that most of the surface samples (0.39–2.07%) and topsoil samples (0.7–1.6%) have clearly lower values than that of the local bedrock material (Qx3 = 1.75%; Qx4 = 2.09%) which indicates a dissolution by weathering processes. Consequently, goethite plays a greater role in the colouring of these samples; this, however, cannot be quantified by this method. The hematite values from the topsoil sections only show a weak positive correlation ($r = 0.41$) with depth yet, with the exception of two samples, a general increase with depth below 20 cm indicates a selective dissolution of hematite upwards. The uppermost samples (0–20 cm) may somehow be affected by surface mixing processes in the soil column. Altogether, the values for total hematite content obtained by this study concur with other findings for soils from the Mediterranean region (Torrent et al., 2007) and other global desert regions (Lafon et al., 2004). However, it should be noted that total hematite contents calculated by this method depend on the applied calibration.

5. Discussion

The results of this current study show a reproducible connection between remote sensing data and laboratory analysis. The remote sensing application provides the possibility to map the spatial distribution of wadi deposits by choosing a specific ASTER band combination of 2/1 as proposed by Rowan and Mars (2003). This enables a clear spatial separation of relocated alluvial sediments and adjacent bedrock which is often problematic in small catchments with a low distance between source and destination of secondary relocated sediments (Bertrams et

Table 7
Signature statistics of the training sites.

Channel	Class 1		Class 2		Class 3		Class 4		Class 5		Class 6		Class 7	
	Mean	Std. dev.	Mean	Std. dev.	Mean	Std. dev.	Mean	Std. dev.	Mean	Std. dev.	Mean	Std. dev.	Mean	Std. dev.
1	163.36	4.39	124.02	4.92	136.21	3.81	197.45	2.794	148.59	2.25	191.64	3.92	185.36	2.61
2	124.85	2.92	94.46	3.82	117.79	4.14	180.85	2.74	136.02	1.88	156.89	4.16	168.55	2.77
3	98.89	5.09	71.07	3.73	93.60	5.04	151.49	3.15	111.60	2.16	126.12	6.83	140.37	3.16
Samples	6587		679		709		533		604		807		246	
Area [m^2]	41,169		4244		4431		3331		3775		5044		615	

Table 8
Classification report.

Name	Pixels	Area [km^2]	% of image	Threshold	Bias
Class 1	385,398	2.41	0.72	3.00	1.00
Class 2	246,919	1.54	0.46	3.00	1.00
Class 3	7,240,041	45.25	13.44	3.00	1.00
Class 4	5,948,120	37.18	11.04	3.00	1.00
Class 5	4,890,933	30.57	9.08	3.00	1.00
Class 6	485,859	3.04	0.90	3.00	1.00
Class 7	6,579,602	41.12	12.22	3.00	1.00
NULL	28,086,172	175.54	52.14		
Total	53,863,044	336.64	100.00		

al., 2012; Bullard and Livingstone, 2002; Weltje and von Eynatten, 2004).

Due to its dry climatic conditions with sparse vegetation cover and the relative homogeneous geology, the study area is well-suited for the combination of digital and classical field studies. Therefore, an elimination of vegetation cover and clouds was not necessary in the remote sensing processing. The geological bedrock substantially supports the mapping of source and destination of weathered iron oxides. For example, the yellow colour in Fig. 3 represents the natural distribution of Fe^{3+} in the Umm Ishrin sandstone.

Some processing features need to be further discussed. Since the resolution of the ASTER image (15 m/pixel with pan-sharpening) and the SPOT-5 image (2.5 m with pan-sharpening) varies, this yields some errors in the applied resampling process for the combination of the images to the target resolution of 15 m. Especially in the resampling of the SPOT-5 data, the originally smooth grid and pixel edges become coarser. Moreover, the edges of the SPOT-5 pixel show some “stairway” effect. This problem may be solved by using high resolution hyperspectral data such as Hymap™ (Cocks et al., 1998).

In detail, the ASTER sensor is suitable for mapping iron oxides by using the band combination B2/B1. However, based on the nature of the spectral characteristic of this band combination, different weathered Fe^{3+} minerals (hematite and goethite) cannot be differentiated. Nonetheless, the output of a high or low value for the Fe^{3+} content can be determined. Here, a possible method is demonstrated to classify the inhomogeneously distributed data by using a standard deviation.

The SPOT-5 image supports the remote sensing analysis of the ASTER image. In the visible colour spectrum of the SPOT-5 data, the red characteristic of the dominant Umm Ishrin sandstone and its weathered sediments are clearly identifiable. Furthermore, the classification of the SPOT-5 data demands a decision concerning which classes represent high contents of Fe^{3+}. In particular, class 3 was excluded from the classification, because it was mainly distributed on the top of the mountains. By choosing the suitable classes for the mapping of the iron oxide content, the right standard deviation is important. The highest correlation was achieved by using a standard deviation of 1.27.

To summarize, it is clear that the remote sensing analysis fundamentally depends on the quality and the resolution of the applied data. Consequently, the grade of preservation of the sediments, directly resulting in different intensities of spectral reflectance, is important and represents a limiting factor of the applied method. At this point, even though the use of higher resolved hyperspectral data (Cocks et al., 1998) is reasonable, the advantage of the applied data is reflected by lower costs.

Overall, the investigated laboratory analysis supports the Fe^{3+} concentrations observed by remote sensing and clearly indicates that the surface samples have experienced secondary alteration compared to the derivative bedrock material. At some sample locations, these weathering processes resulted in a decrease in hematite content and, thus, an increase in the effect of goethite on the colouring of these deposits. However, weathering intensities generally have to be classified as initial due to the low amounts of seasonal rainfall and insufficiency of microbial activity and formation of organic matter. The results agree with results from Schwertmann and Lentze (1966) who found that hematite generally dominates the colour of natural samples with hematite–goethite mixtures if it is present in specific amounts, inducing a reddish colouring. Yellow colours only predominate if the hematite content sinks below a specific level, e.g. due to weathering processes and a preferred development of goethite. The continuum removed absorption spectrum (Fig. 8) clearly shows that most samples are dominated by hematite mixed with minor amounts of goethite. Hence, it is interpreted that the local bedrock sandstone contains Fe^{3+} in the form of hematite ($Fe^{(3+)}{}_2O_3$), which is responsible for the red colouring. Due to surface weathering processes, increasingly more iron is transformed from Fe^{2+} to Fe^{3+} (primary hematite) by oxidation. As a result of chemical affiliation of water or a selective dissolution of hematite, goethite ($Fe^{(3+)}O(OH)$) might then gain influence in the colouring of some samples in a further step. However, results from three investigated subsurface trenches depict minor stages of weathering and secondary alteration of iron oxides which is probably related to insufficient rainfall infiltration and inhibited carbonate leaching under the recent climatic conditions.

The results of the remote sensing and laboratory analysis are intended for estimating possible new archaeological sites. Recently there have been two basic approaches of archaeological prospection: the inductive and the deductive method. The inductive approach is

Table 9
Confusion matrix.

Areas as per cent pixels classified by code										
Name	Code	Pixels	0	1	2	3	4	5	6	7
Class 1	1	6587	4.71	95.26	0	0.02	0	0	0.02	0
Class 2	2	679	3.53	0	95.43	1.03	0	0	0	0
Class 3	3	709	4.80	0	0	94.50	0	0.71	0	0
Class 4	4	533	4.69	0	0	0	94.93	0	0	0.38
Class 5	5	604	3.97	0	0	0.33	0	95.70	0	0
Class 6	6	807	3.72	0	0	0	0	0	95.79	0.50
Class 7	7	246	4.47	0	0	0	0	0	1.63	93.9
Average accuracy	95.07%									
Overall accuracy	95.24%									
Kappa coefficient	0.91768									
Confidence level										
Standard deviation	0.0036									
99%	0.91768 ± 0.00928									
95%	0.91768 ± 0.00705									
90%	0.91768 ± 0.00591									

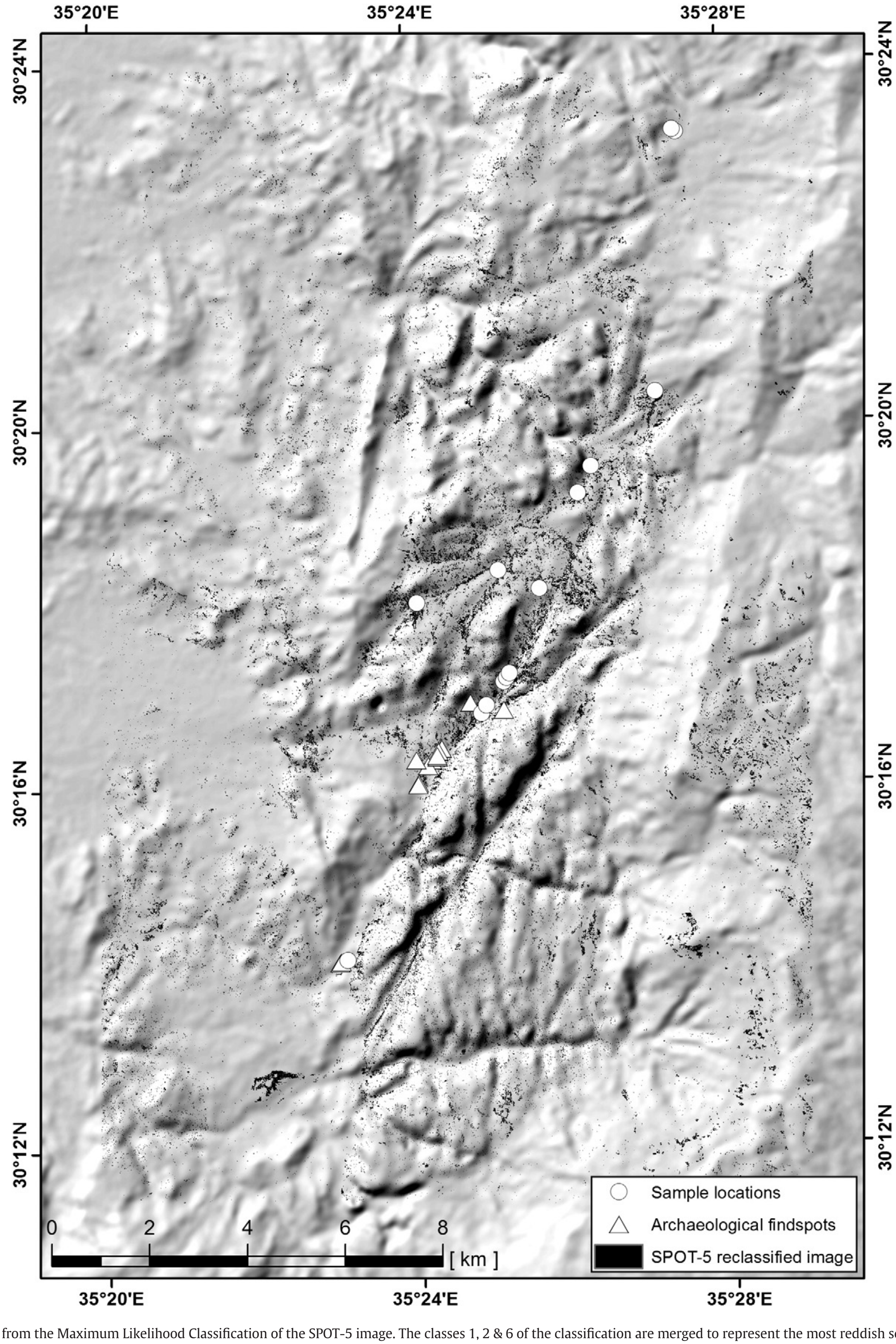

Fig. 5. Results from the Maximum Likelihood Classification of the SPOT-5 image. The classes 1, 2 & 6 of the classification are merged to represent the most reddish sediments in the area of investigation.

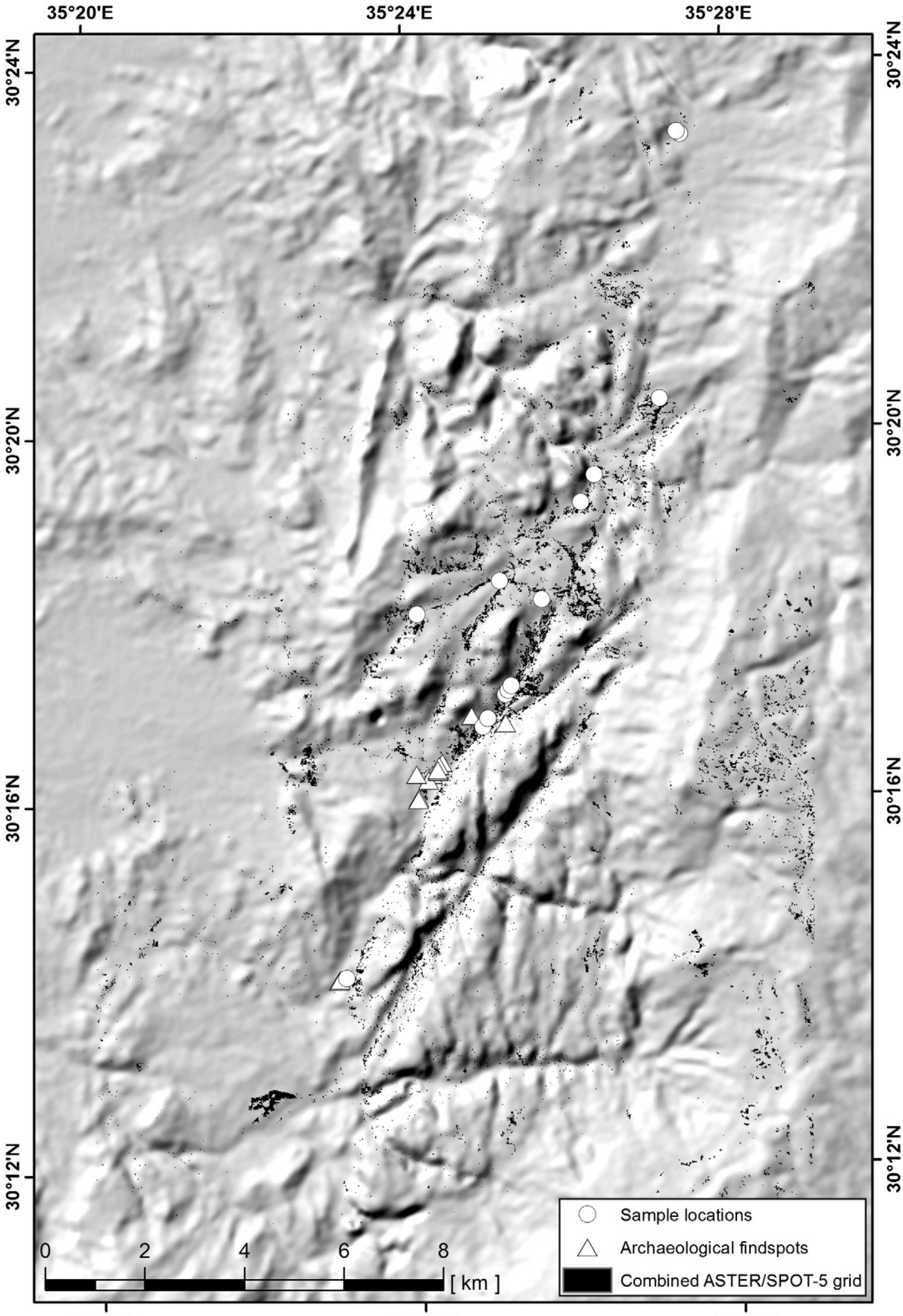

Fig. 6. The conditional function supports the results from the ASTER and SPOT-5 mapping. This result shows possible areas of high Fe^{3+} content and respectively surface structures which are similar to the known archaeological find spots.

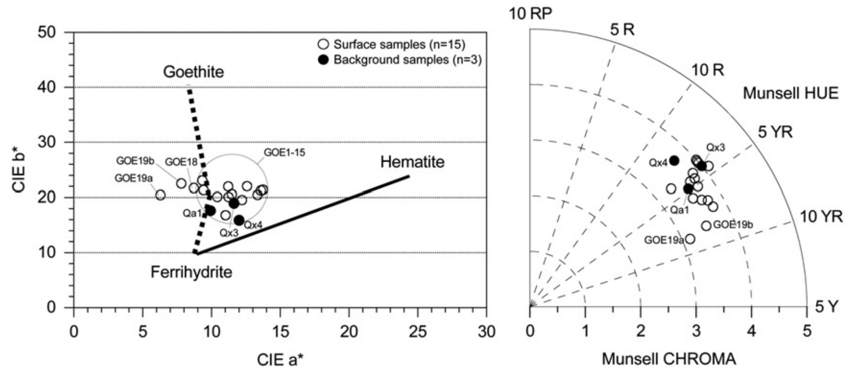

Fig. 7. Bivariate plot of the CIE a* and b* values (according to Nagano et al., 1994) for all investigated surface samples and Munsell data in the YR colour range (according to Schwertmann and Cornell, 2000).

controlled by landscape parameters such as geomorphometric features, soils and hydrologic data. The deductive approach is based on knowledge of experts who build the prediction model (e.g. Finke et al., 2008). For both methods an adequate database is needed. Often the archaeological record is either too dense for geostatistic interpolation or concentrates in certain areas. At a low density of archaeological sites, a point-area interpolation provides inexact prediction in those areas where records are missing. In this current study, it is possible to identify potential archaeological find spots based on their remote sensing and spectral information. However, it should be noted that human settlement strategies are generally not affected by physical properties of the sediment but rather are linked to biotic features of the landscape

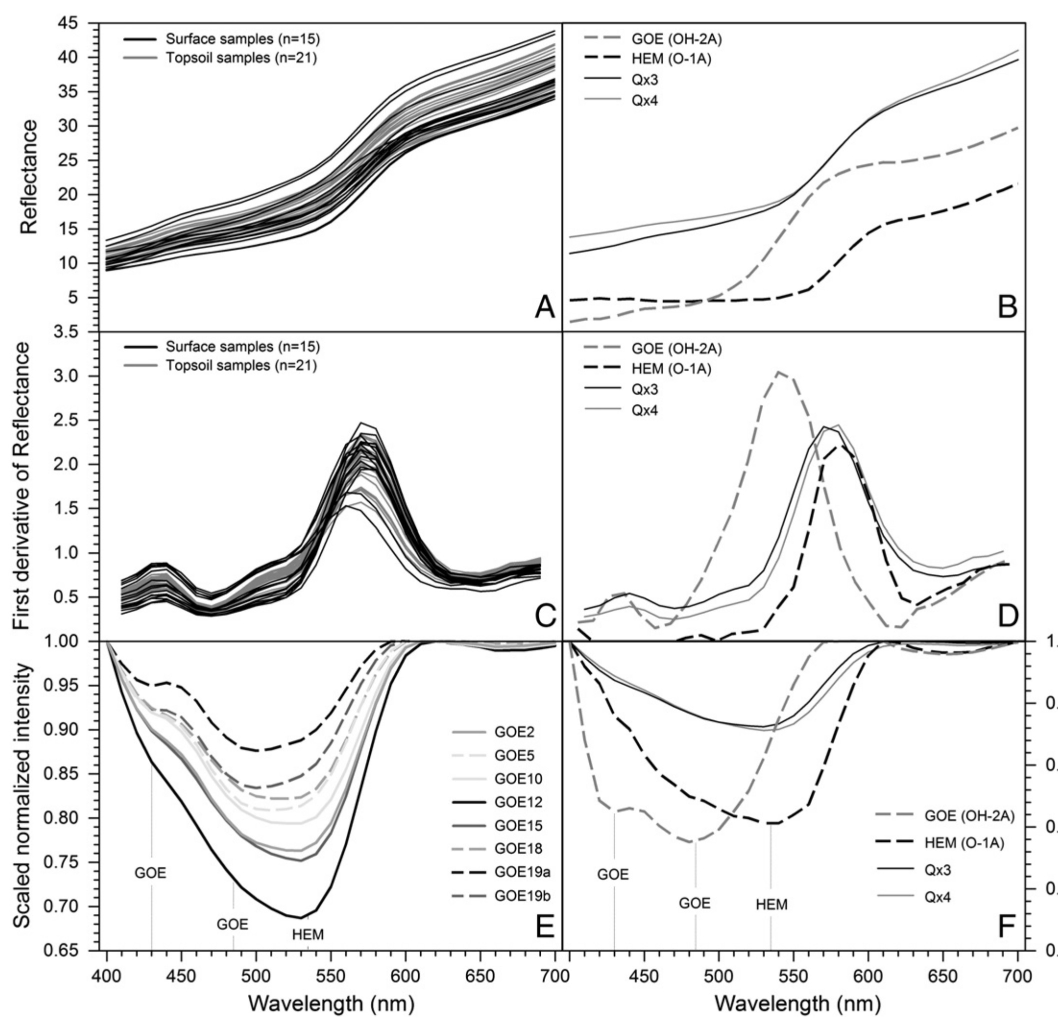

Fig. 8. Results from VIS-spectroscopy: (A) Visible reflectance spectra of all surface and topsoil samples. (B) Visible reflectance spectra of synthetic samples of hematite (O-1A)* and goethite (OH-2A)* and bedrock samples (Qx3, Qx4). (C) First derivative of VIS-spectra for all surface and topsoil samples. (D) First derivative of VIS-spectra for synthetic iron oxides* and bedrock samples. (E) Scaled normalised reflectance intensity for selected surface samples, synthetic iron oxides* and geologic samples (F) after applying the continuum removal analysis on the visible reflectance spectra. Dashed lines indicate characteristic peaks of specific iron oxides. (*data: Grove et al., 1992; Baldridge et al., 2009).

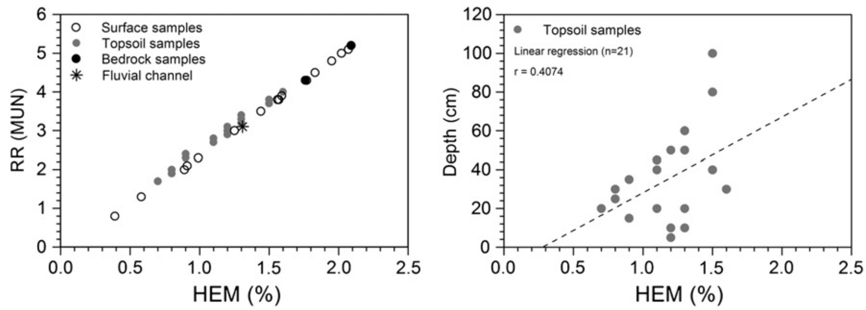

Fig. 9. Estimated hematite contents from the Redness Rating index (according to Torrent et al., 1983) for surface, topsoil and background samples from the study area.

such as the presence of food, shelter, and water. Even so, the investigated sedimentary deposits appear to be the terrestrial archive with the highest potential for a preservation of archaeological sites in arid environments like the Levantine region. Combined with the aforementioned factors, the method presented here might be exploited to more precisely estimate new archaeological find spots in future investigations.

6. Conclusion

In the present study, Palaeolithic sites were recorded on top or within reddish wadi deposits of Pleistocene age in a small wadi catchment in Southern Jordan (c.f. Bertrams et al., 2012). With the applied methodology, it was possible to map the distribution of wadi sediments having similar characteristics as the ones embedding already known sites. An attribute that was easily to map from remote sensing data was the Fe^{3+} content of surface sediments, which also indicates the degree of weathering. The discrimination between high and low values of iron oxides reflected the relief of the study area and clearly delineated the sediments from its bedrock source. Additionally, the usage of ASTER and SPOT-5 images and the analysis of various spectral channels resulted in a more detailed mapping. The data aggregates in every step of the digital analysis. Finally specific areas with the known surface characteristic from the archaeological findings could be identified.

Direct measurements of VIS-spectra on selected surface samples from the study area supported the evidence of iron oxide weathering at the recent surface obtained by remote sensing and provided insights into pedogenic processes (Ben-Dor et al., 2002). The results documented distinct yet initial processes of Fe^{3+} release and secondary alteration from the primary hematite-dominated bedrock material induced by chemical dissolution. Some samples even showed an advanced degree of goethite formation that is most probably induced by a selective dissolution of hematite as proven by calculated contents for this iron oxide from the redness rating index. However, additional topsoil sections from different parts of the study area did not point to an advanced state of weathering. The applied laboratory analysis thus supported information about weathering intensities under near-surface conditions in the recent arid environment. This, in turn, supported the remote sensing analysis by delivering information about the quantity and quality of iron oxides in the analysed bedrock and sediments.

This combined approach of remote sensing and VIS-spectroscopy enables a mapping of areas having the same spectral characteristics as the archaeological sites. Thus, researchers can predict new potential find spots for archaeological sites by investigating regions of comparable catchments with homogeneous sandstone geology, derivative sediments and consistent spectral information. A systematic archaeological prospection at these sites is part of future work. Additionally, we intend to extend our research by focusing on the potential to reconstruct palaeoenvironmental conditions from the geochemical characteristics of the ancient wadi fills.

Acknowledgements

This study is part of the multidisciplinary Collaborative Research Centre (CRC) 806 "Our Way to Europe" which is funded by the German Research Foundation (Deutsche Forschungsgemeinschaft; DFG). Eileen Eckmeier is funded by the DFG-project EC 401/1-1. Special thanks go to our colleague Dr. D. Schyle from the Department of Archaeology, University of Cologne and to Prof. Dr. M. Baales (Ruhr-University Bochum) for providing Fig. 1.

Fieldwork 2009 and 2010 took place in close cooperation with the Department of Antiquities (DOA) of Jordan. We are greatly indebted to the Director General of the Department, Dr. Ziad al-Saad (2010), for the continuous support of the project. In particular, we profited much from the generous help of the DOA representatives in the field (Tallal al-Ammarin, Mohammed Abd-al-Aziz Marahleh, Amer Bdour, Adnan Rafayah, Hussein Dahbour) and various administrative advice and assistance kindly provided by Khalil Hamdan (DOA Amman).

We also are most grateful to two anonymous reviewers for detailed comments that led us to significantly improve the manuscript. A special thank goes to M.-J. Blümich for the English editing of the manuscript.

References

Abrams, M., 2000. The advanced spaceborne thermal emission and reflection radiometer (ASTER): data products for the high spatial resolution imager on NASA's Terra platform. International Journal of Remote Sensing 21, 847–859.

Abrams, M., Hook, S.J., 1995. Simulated Aster data for geological studies. IEEE Transactions on Geoscience and Remote Sensing 33, 692–699.

ASTER GDEM, 2010. These data are distributed by the Land Processes Distributed Active Archive Center (LP DAAC), located at the U.S. Geological Survey (USGS). Earth Resources Observation and Science (EROS) Center. (lpdaac.usgs.gov).

Baldridge, A.M., Hook, S.J., Grove, C.I., Rivera, G., 2009. The ASTER spectral library version 2.0. Remote Sensing of Environment 113, 711–715.

Barjous, M.O., 2003. The geology of Petra and Wadi al Lahyana area, map sheets No. 3050-I and 3050-IV. The Hashemite Kingdom of Jordan Natural Resources Authority, Geology Directorate, Geological Mapping Division Amman. Bulletin 56 (96 pp.).

Bar-Yosef, O., 2002. The Upper Paleolithic revolution. Annual Review of Anthropology 31, 363–393.

Bar-Yosef, O., van der Meersch, B., Arensburg, B., 1986. New data on the origin of modern man in the Levant. Current Anthropology 27, 63–64.

Ben-Dor, E., Levin, N., Singer, A., Karnieli, A., Braun, O., 2002. Quantitative mapping of the soil rubification process on sand dunes, using field and airborne sensors. AVIRIS Airborne Geoscience Workshop Proceedings 2002.

Ben-Dor, E., Levin, N., Singer, A., Karnieli, A., Braun, O., Kidron, G.J., 2006. Quantitative mapping of the soil rubification process on sand dunes using an airborne hyperspectral sensor. Geoderma 131, 1–21.

Bertrams, M., Protze, J., Löhrer, R., Schyle, D., Richter, J., Hilgers, A., Klasen, N., Schmidt, C., Lehmkuhl, F., 2012. Multiple environmental change at the time of the Modern Human passage through the Middle East: first results from geoarcheological investigations on Upper Pleistocene sediments in the Wadi Sabra (Jordan). Quaternary International 274, 55–72.

Bhattacharyya, A., 1943. On a measure of divergence between two statistical populations defined by their probability distributions. Bulletin of the Calcutta Mathematical Society 35, 99–109.

Bierwirth, P.N., 1990. Mineral mapping and vegetation removal via data-calibrated pixel unmixing, using multispectral images. International Journal of Remote Sensing 11, 1999–2017.
Bullard, J.E., Livingstone, I., 2002. Interactions between aeolian and fluvial systems in dryland environments. Area 34, 8–16.
Clark, R.N., King, T.V.V., Gorelick, N.S., 1987. Automatic continuum analysis of reflectance spectra. Proceedings of the Third AIS Workshop, 2–4 June 1987. : JPL Publication, 87(30). Jet Propulsion Laboratory, Pasadena, pp. 138–142.
Cocks, T., Jenssen, R., Stewart, A., Wilson, I., Shields, T., 1998. The HYMAP™ Airborne Hyperspectral Sensor: the System, Calibration and Performance. 1st EARSEL Workshop on Imaging Spectroscopy, Zurich.
Commission Internationale de l'Eclairage (CIE), 1978. Recommendations on uniform color spaces, color-difference equations, psychometric color terms. Publication CIE No. 15 (E- 1.3.1), Supplement 2.Bureau Central de la CIE, Paris, France.
Cornell, R.M., Schwertmann, U., 2003. The Iron Oxides — Structure, Properties, Reactions, Occurrences and Uses. Wiley-VCH, Weinheim.
Crowley, J.K., 1993. Mapping playa evaporite minerals with AVIRIS data: A first report from Death Valley, California. Remote Sensing of Environment 44, 337–356.
Defries, R.S., Townshend, J.R.G., 1994. NDVI-derived land cover classifications at a global scale. International Journal of Remote Sensing 15, 3567–3586.
Finke, P.A., Meylemans, E., Van de Wauw, J., 2008. Mapping the possible occurence of archaeological sites by Bayesian inference. Journal of Archaeological Science 35, 2786–2796.
Folk, R.L., 1976. Reddening of desert sands: Simpson Desert, N.T., Australia. Journal of Sedimentary Petrology 46 (3), 604–615.
Gardner, R.A.M., 1981. Reddening of dune sands — evidence from southeast India. Earth Surface Processes and Landforms 6, 459–468.
Gebel, H.-G., 1983. Sabra 1 und die Wadisysteme um Petra/Wadi Musa. Archiv für Orientforschung 29/30, 282–284.
Gebel, H.-G., 1988. Late Epipalaeolithic–Aceramic Neolithic sites in the Petra-Area. In: Garrard, A.N., Gebel, H.-G. (Eds.), The Prehistory of Jordan. The State of Research in 1986. : British Archaeological Reports, International Series, 396i. Archaeopress, Oxford, pp. 67–100.
Grove, C.I., Hook, S.J., Paylor, E.D., 1992. Laboratory reflectance spectra of 160 minerals, 0.4 to 2.5 micrometers. JPL Publication, 92. Jet Propulsion Laboratory, Pasadena.
Grunert, J.W., Völkel, J., Leopold, M., 2007. Reconstruction of changes in fluvial regime using sediments from Wadi Morikh, South Sinai (Egypt), first results. In: Tooth, S., Woodward, J.C. (Eds.), 4th International Palaeoflood Workshop, 24.–30.06.2007 Crete/Greece, p. 36.
Hewson, R.D., Cudahy, T., Huntington, J., 2001. Geologic and alteration mapping at Mt. Fitton, South Australia, using ASTER satellite-borne data. Geoscience and Remote Sensing Symposium, 2001 (IGARSS '01): IEEE 2001 International, pp. 724–726.
Hewson, R.D., Cudahy, T.J., Drake-Brockman, J., Meyers, J., Hashemi, A., 2006. Mapping geology associated with manganese mineralization using spectral sensing techniques at Woodie Woodie, East Pilbara. Exploration Geophysics 37, 389–400.
Hubbard, B.E., Rowan, L.C., Dusel-Bacon, C., Eppinger, R.G., 2007. Geologic mapping and mineral resource assessment of the Healy and Talkeetna Mountains quadrangles, Alaska using minimal cloud- and snow-cover ASTER data. U.S. Geological Survey Open-File Report 2007–1046, Boulder Colorado, p. 22.
Hublin, J.J., 2009. The origin of Neanderthals. Proceedings of the National Academy of Sciences of the United States of America 106, 16022–16027.
Kalinowski, A., Oliver, S., 2004. ASTER mineral index processing. Remote Sensing Application Geoscience Australia.Australian Government Geoscience (http://www.ga.gov.au/image_cache/GA7833.pdf (access 12.10.2012)).
Lafon, S., Rajot, J.-L., Alfaro, S.C., Gaudichet, A., 2004. Quantification of iron oxides in desert aerosol. Atmospheric Environment 38, 1211–1218.
Lillesand, T.M., Kiefer, R.W., Chipman, J.W., 2004. Remote Sensing and Image Interpretation. Wiley, Chichester.
Makhlouf, I.M., Abed, A.M., 1991. Depositional facies and environments in the Umm Ishrin Sandstone Formation, Dead Sea area, Jordan. Sedimentary Geology 71, 177–187.
Mars, J.C., Rowan, L.C., 2006. Regional mapping of phyllic- and argillic-altered rocks in the Zagros magmatic arc, Iran, using Advanced Spaceborne Thermal Emission and Reflection Radiometer (ASTER) data and logical operator algorithms. Geosphere 2, 161–186.
Mars, J.C., Rowan, L.C., 2011. ASTER spectral analysis and lithologic mapping of the Khanneshin carbonite volcano, Afghanistan. Geosphere 7, 276–289.
Mathieu, R., Pouget, M., Cervelle, B., Escadafal, R., 1998. Relationships between satellite-based radiometric indices simulated using laboratory reflectance data and typic soil colour of an arid environment. Remote Sensing of Environment 66, 17–28.
Mellars, P., 2004. Neanderthals and the modern human colonization of Europe. Nature 432, 461–465.
Mellars, P., 2006. Why did modern humans populations disperse from Africa ca. 60,000 years ago? A new model. Proceedings of the National Academy of Sciences of the United States of America 103, 9381–9386.
Mickus, K., Johnson, E., 2001. Mapping sedimentary and volcanic units within and surrounding Petrified Forest National Park, Arizona, using Landsat-5 and SPOT panchromatic data. Remote Sensing 22, 1919–1935.
Munsell Color Company Inc., 1975. A Color Notation: An Illustrated System Defining All Colors and Their Relations by Measured Scales of Hue, Value, and Chroma. Gould Library, Baltimore.
Nagano, T., Nakashima, S., Nakayama, S., Senoo, M., 1994. The use of color to quantify the effects of pH and temperature on the crystallization kinetics of goethite under highly alkaline conditions. Clays and Clay Minerals 42, 226–234.
Ninomiya, Y., Fu, B., 2001. Spectral indices for lithologic mapping with ASTER thermal infrared data applying to a part of Beishan Mountains, Gansu, China. Geoscience and Remote Sensing Symposium, 2001 (IGARSS '01). IEEE 2001 International, pp. 2988–2990.
Temporal and spatial corridors of *Homo sapiens sapiens* population dynamics during the late Pleistocene and early Holocene. In: Richter, J., Melles, M., Schäbitz, F. (Eds.), Quaternary International, 274 (272 pp.).
Rowan, L.C., Mars, J.C., 2003. Lithologic mapping in the Mountain Pass, California area using advanced spaceborne thermal emission and reflection radiometer (ASTER) data. Remote Sensing of Environment 84, 350–366.
Rowan, L.C., Hook, S.J., Abrams, M.J., Mars, J.C., 2003. Mapping hydrothermally altered rocks at Cuprite, Nevada, using the advanced spaceborne thermal emission and reflection radiometer (ASTER), a new satellite-imaging system. Economic Geology 98, 1019–1027.
Royal Jordanian Geographic Centre, 2007. Atlas of Jordan and the World 2007 (128 pp.).
Scheinost, A.C., Schwertmann, U., 1999. Color identification of iron oxides and hydroxysulfates: use and limitations. Soil Science Society of America Journal 63, 1463–1471.
Scheinost, A.C., Chavernas, A., Barrón, V., Torrent, J., 1998. Use and limitations of second-derivative diffuse reflectance spectroscopy in the visible to near-infrared range to identify and quantify Fe oxide minerals in soils. Clays and Clay Minerals 46, 528–536.
Schwertmann, U., 1959. Die fraktionierte Extraktion der freien Eisenoxyde in Böden, ihre mineralogischen Formen und ihre Entstehungsweisen. Zeitschrift für Pflanzenernährung, Düngung und Bodenkunde 84, 194–204.
Schwertmann, U., 1966. Inhibitory effect of soil organic matter on the crystallization of amorphous hydroxide to goethite. Nature 212, 645–646.
Schwertmann, U., 1969. Der Einfluss einfacher organischer Anionen auf die Bildung von Goethit und Hämatit aus amorphem Fe(III)-Hydroxid. Geoderma 3, 207–214.
Schwertmann, U., Cornell, R.M., 2000. Iron Oxides in the Laboratory — Preparation and Characterization. Wiley-VCH, Weinheim.
Schwertmann, U., Lentze, W., 1966. Bodenfarbe und Eisenoxidform. Journal of Plant Nutrition and Soil Science 115, 209–214.
Schyle, D., Uerpmann, H.-P., 1988. Paleolithic sites in the Petra Area. In: Garrard, A.N., Gebel, H.-G. (Eds.), The Prehistory of Jordan. The State of Research in 1986, 39–65. : British Archaeological Reports, International Series, 396i. Archaeopress, Oxford, pp. 67–100.
Shafique, M., van der Meijde, M., Rossiter, D.G., 2011a. Geophysical and remote sensing-based approach to model regolith thickness in a data-sparse environment. Catena 87, 11–19.
Shafique, M., van der Meijde, Ullah, S., 2011b. Regolith modeling and its relation to earthquake induced building damage: a remote sensing approach. Journal of Asian Earth Sciences 42, 65–75.
Sherman, D.M., Waite, T.D., 1985. Electronic spectra of Fe^{3+} oxides and oxide hydroxides in the near IR to near UV. American Mineralogist 70, 1262–1269.
SPOT IMAGE, 2011. Resolutions and spectral modes. SPOT-5 Technical Information. http://www.satimagingcorp.com/satellite-sensors/SPOT-5_Resolution_Spectral_Modes.pdf (access 12.10.2012).
Stringer, C., 2002. Modern human origins: progress and prospects. Philosophical Transactions of the Royal Society 357, 563–579.
Torrent, J., Barrón, V., 1993. Laboratory measurement of soil colour. Theory and practice. Soil Science Society of America Journal, Special Publication 31, 21–33.
Torrent, J., Schwertmann, U., Fechter, H., Alferez, F., 1983. Quantitative relationships between soil colour and hematite content. Soil Science 136, 354–358.
Torrent, J., Liu, Q., Bloemendal, J., Barrón, V., 2007. Magnetic enhancement and iron oxides in the Upper Luochuan loess-paleosol sequence, Chinese Loess Plateau. Soil Science Society of America Journal 71, 1570–1578.
Walker, T.R., 1974. Formation of red beds in moist tropical climates: a hypothesis. Geological Society of America Bulletin 8, 633–638.
Weltje, G.J., von Eynatten, H., 2004. Quantitative provenance analysis of sediments: review and outlook. Sedimentary Geology 171, 1–11.
Yamaguchi, Y., Kahle, A.B., Tsu, H., Kawakami, T., Pniel, M., 1998. Overview of advanced spaceborne thermal emission and reflection radiometer (ASTER). IEEE Transactions on Geoscience and Remote Sensing 36, 1062–1071.